Supplementary Materials for

Robust topological BIC nanocavities for upconversion directional emission

Yongqi Chen[1], Ming Zhu[2], Qingfeng Bian[1], Xiumei Yin[3], Wenxin Wang[2, *], Bin Dong[3,*], and Yurui Fang[1, *]

[1.] *School of Physics, Dalian University of Technology, Dalian 116024, China.*

[2.] *Qingdao lnnovation and Development Center, Harbin Engineering University, Qingdao, 266500, China*

[3.] *School of Physics and Materials Engineering, Dalian Nationalities University, Dalian 116600, China*

**Corresponding authors: wenxin.wang@hrbeu.edu.cn (W.W), dong@dlnu.edu.cn (B.D.), yrfang@dlut.edu.cn (Y.F.)*

Contents

1. Undeformed and TPC lattice Γ point mode profiled

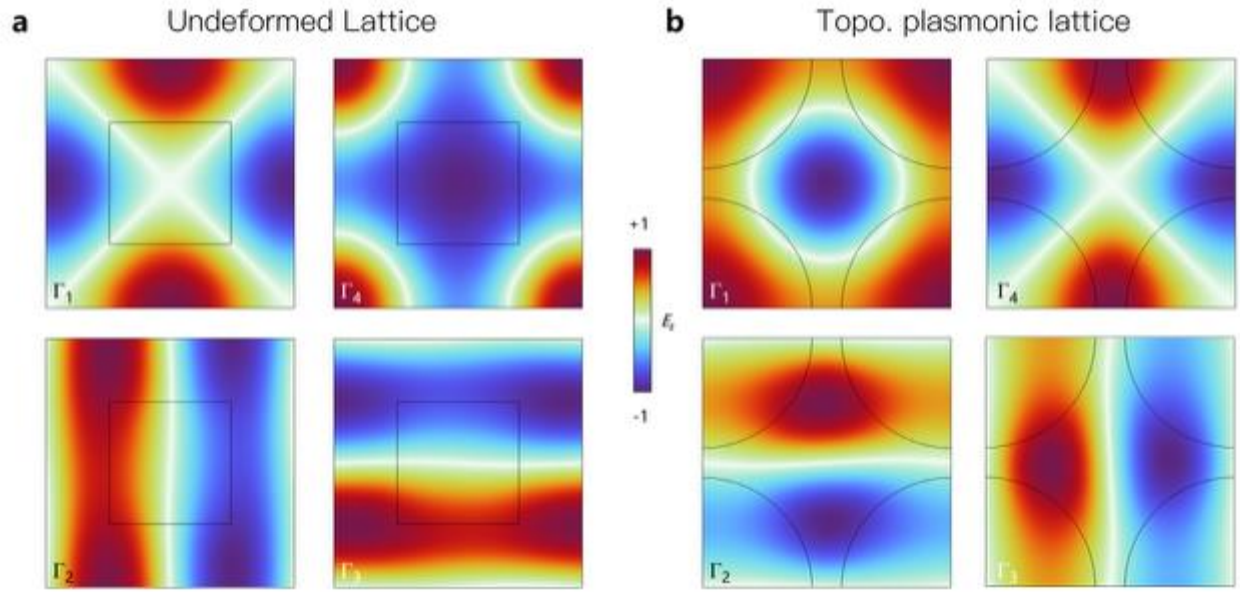

Supplementary Fig. S1 Shows the mode distributions at the Γ point for undeformed (a) and plasmonic lattices (b) under periodic boundary conditions. To reveal the symmetry-protected BIC, we calculated the eigenfrequencies of both lattices located at the Γ point. These mode distributions illustrate the normalised *z* component of the electric field E_z in the lattice *xy* plane. **a,** In aluminium photonic crystal plates, the undeformed lattice (lattice constant a = 400 nm , air-hole edge length r = 0.49a , height H = 300 nm) exhibits two BIC modes Γ_1/Γ_4, decoupled under C_2 symmetry. **b,** For the uncompressed plasmonic lattice (Δr = 0.45a), the quadrupole mode Γ_1 appears in the low-frequency branch, two coupled dipole modes in Γ_2/Γ_3, and a monopole mode (Γ_4) at the Γ point in the upper band.

2. The measured *Q* factor and the calculated effective mode volume V_{eff}

To further evaluate the optical performance of the TPC, we performed experimental characterization of the quality factor (Q) and numerical calculated of the effective mode volume (V_{eff}).

2.1 Experimental Q factor calculation results

The experimental Q-factor was extracted from angle-resolved scattering measurements of the fabricated nanocavity arrays. Since the ideal BIC mode at the Γ point is non-radiative, the Q-factor was determined from the quasi-BIC (q-BICs) resonance at a small off-axis angle (1°). By applying a Lorentzian fit to the scattering resonance, the experimental Q-factor is defined as:

$$Q = \frac{\lambda_0}{\Delta\lambda}$$

where λ_0 is the resonance peak wavelength and $\Delta\lambda$ is the full width at half maximum, and a full width at half maximum of $\Delta\lambda = 2.52$ nm. The measured experimental Q-factor was determined to be 219.72. The experimental data and fitted curve are presented in Fig. S2. The deviation from the numerical prediction ($Q \approx 467.4$) is attributed to radiative loss away from the singular Γ point and fabrication-related damping.

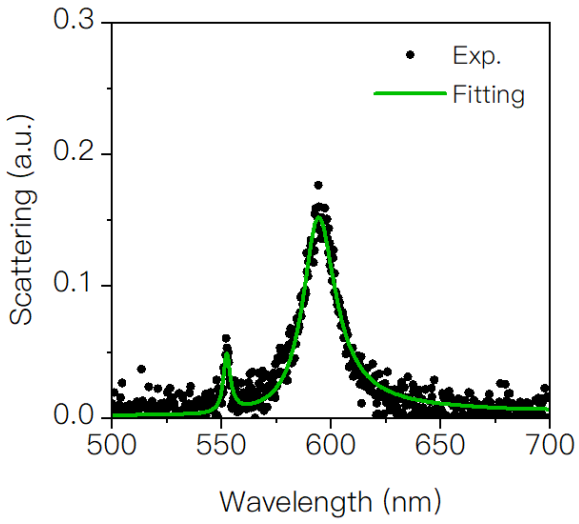

Supplementary Fig. S2. Measured ARSS of the TPC at 1° collection angle. Lorentzian fitting of the resonance at λ_0 = 551.2 nm.

2.2 TPC effective mode volume

The effective mode volume was calculated using the COMSOL Multiphysics to quantify the spatial confinement of the electromagnetic field, defined as:

$$V_{eff} = \frac{\iiint \varepsilon(\mathbf{r})|\mathbf{E}(\mathbf{r})|^2 d^3r}{\max[\varepsilon(\mathbf{r})|\mathbf{E}(\mathbf{r})|^2]}$$

Our TPC system exhibits a synergistic dual-mode resonance, characterized by two distinct mode volumes: LSPR, Concentrated at the nanocone tip, providing an extremely small mode volume of approximately 1.24×10^4 nm^3. This localized hotspot is the primary driver for near-field enhancement. Topological BIC Cavity Mode, Distributed across the nanocavity array, characterized by a larger but highly coherent mode volume of approximately 3.8×10^7 nm^3, which governs the collective resonance and far-field directionality.The combination of these two modes ensures both extreme field localization and efficient far-field coupling.

2.2.1 Spatial overlap of different size NCs with the cavity affects Purcell enhancement

To provide a physical grounding for the size-dependent radiative rate modifications observed in Fig. 5h, we performed an analytical estimation of the spatial overlap between the nanocrystal (NC) volume and the cavity's electromagnetic mode. The overall enhancement M can be qualitatively approximated by $M=F\times|E|^2$, where F is the Purcell factor determined by the optical local density of states(*1*). So, for certain size of particle, $M \propto \iiint_{V_{NP}} |E|^2 \, dV$. For an extended emitter such as an upconversion NC, the effective enhancement is the volume integral of the local field distribution over the particle's physical dimensions.

Smaller NC sizes result in a reduced spatial overlap with the enhancement center and a smaller integral volume within the mode field. Based on the calculated effective mode volume ($Veff = 3.8\times10^7$ nm³), the 400 nm NC possesses a physical volume of approximately 3.35×10^7 nm³, representing a mode occupancy of 88% and a corresponding Purcell factor of 18.3. In contrast, the 300 nm NC occupies a volume of 1.41×10^7 nm³ (37% occupancy) with a Purcell factor of 9.89, while the 200 nm NC occupies only 0.42×10^7 nm³ (11% occupancy) with a Purcell factor of 9.07.

3. Experimental samples

3.1 Undeformed cavity and plasmonic cavity fabrication

High-purity aluminum foil is cleaned using a solution of acetone and ethanol to remove surface impurities and oxides. The aluminum foil is then electropolished to create a smooth surface, providing a uniform base for the subsequent anodization process. As show in the S3a, a two-step anodisation method is used to prepare the tetragonal lattice aluminium photonic crystal hole plate (S3b). In the first step, anodisation is performed under appropriate voltage conditions to form an anodised aluminium oxide (AAO) template layer on the aluminium photonic crystal plate. Subsequently, the initial AAO layer is completely dissolved in a chromic acid solution to expose a smooth and structurally regular aluminium surface.

In a second anodizing step, the aluminum surface is further anodized under the same voltage conditions, resulting in the formation of a highly ordered tetragonal AAO pore lattice(*2*). By adjusting the anodization voltage, duration, and electrolyte composition, the pore size, wall thickness, and overall thickness of the AAO template can be controlled. To form the periodic barrier layer at the bottom of the triangular lattice AAO template, anodization is continued until the pore growth stabilizes. Finally, the top oxide layer was removed by wet chemical etching to expose the plasmonic lattice array on the aluminium substrate (S3**S3**c).

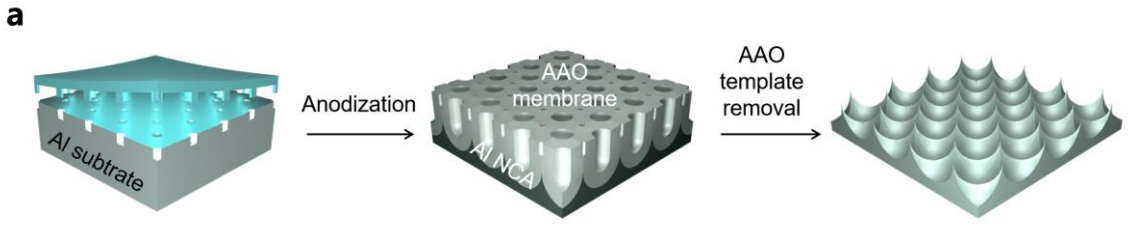

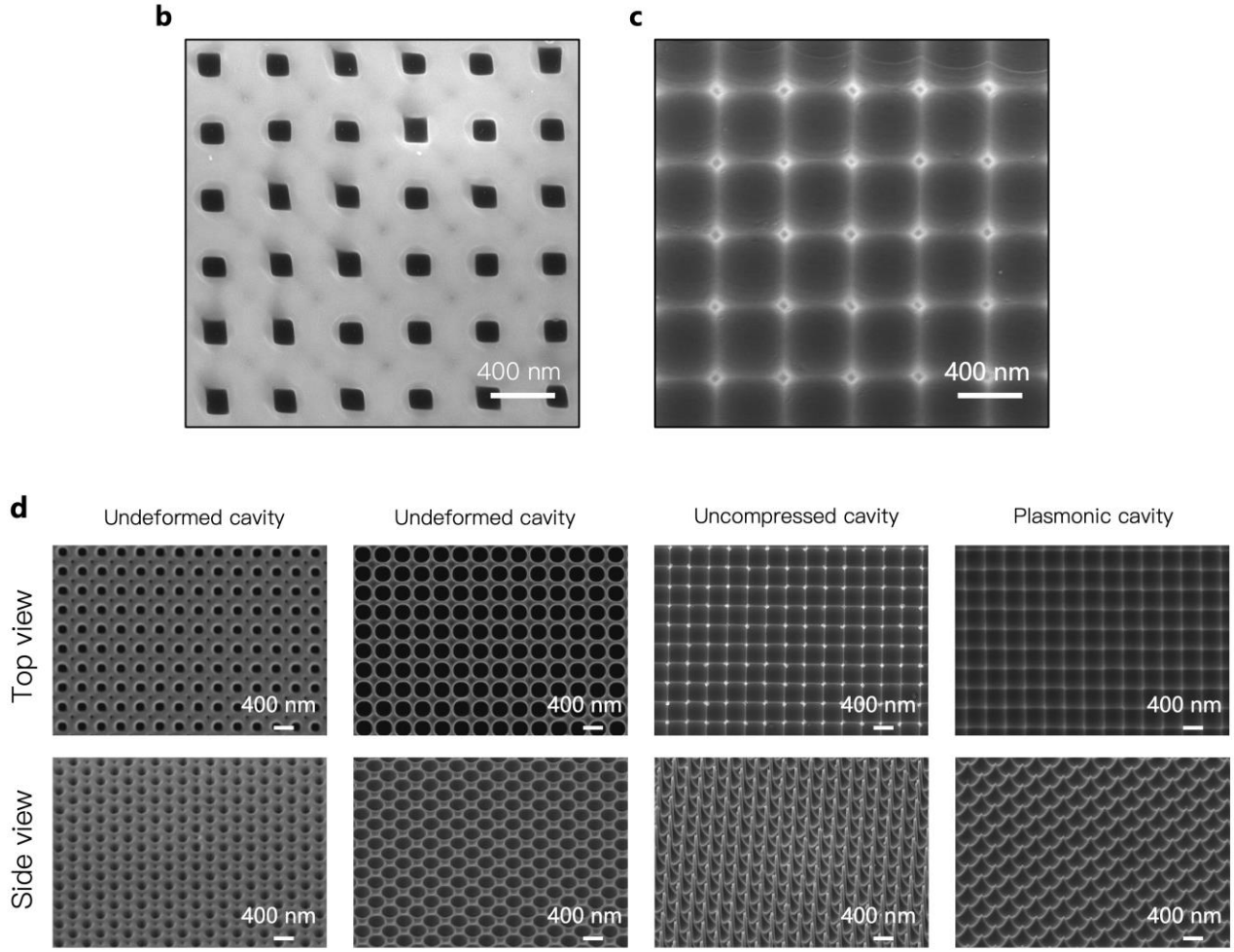

Supplementary Fig. S3 (a) illustrates the fabrication process of periodic Al-NCA with a 400 nm lattice constant, realized through a combination of pre-imprinting and anodic oxidation. The corresponding SEM image of undeformed aluminium photonic crystal hole plates **(b)** and plasmonic cavity lattice arrays **(c)** with lattice constant *a* = 400 nm from a perspective view. **(d)** The SEM image showing the required cavity geometry as the reaction proceeds

3.1.1 Atomic force microscopy (AFM) image of the topological plasmonic cavity.

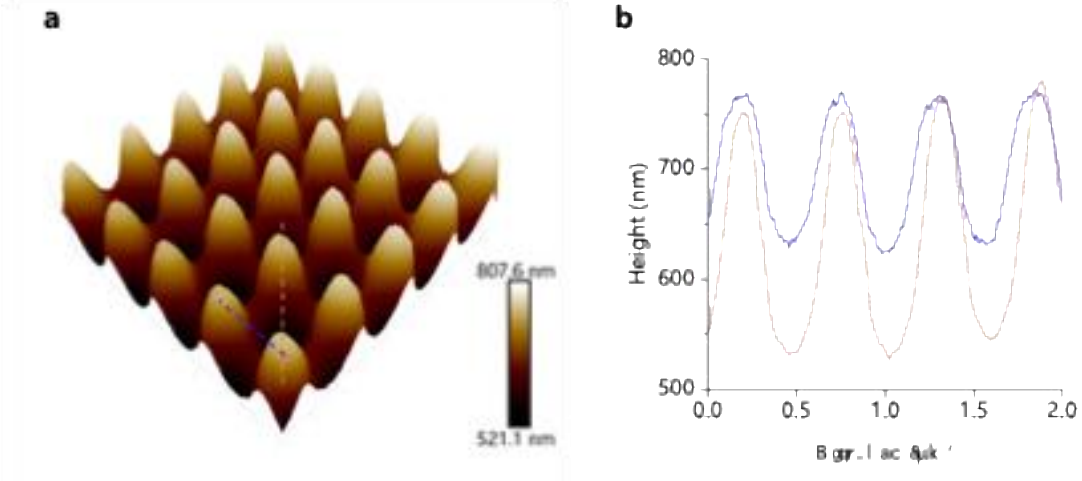

Supplementary Fig. S4. a, AFM three-dimensional image of the topological plasmonic cavity. **b,** The solid orange line shows the *XZ* height profile scanned along the diagonal path of the grid (the orange dashed line in (a)), revealing a height difference of 210 nm. The blue solid line shows the *XZ* height profile scanned along the direction of the right-angle side (blue dashed line in (a)).

3.2 Upconversion NCs sample information

3.2.1 Synthesis of $NaYF_4$:10% Yb^{3+}, 2% Er^{3+}@$NaYF_4$ core-shell NCs

3 mL oleic acid and 7 mL octadecene were added to the two vials respectively, and 2 mL $Re(CH_3COO)_3$ (0.2 M) was added in proportion (where Re = Y^{3+}, Yb^{3+}, and Er^{3+} in a molar ratio of 88:10:2). The samples present pale yellow after heating to 150 °C and preservation for 45 min, a rare earth oleate precursor solution can be obtained while the sample was cooled to room temperature. 1 mL NaOH (1M) and 4 mL NH_4F (0.4 M) methanol mixture were added to the solution, insulated at 50 °C for 40 min. Vacuumed at 100 ℃ and argon was swap every 3 min to balance bottle pressure. The solution was quick heated (15 min) to 290 ℃ when bubble no longer produced, kept warm for 1.5 h, and desired product can obtain while cooled to room temperature. The nanoparticles with different size were synthesized at different temperature. A certain amount of ethanol solution was added to the solution, centrifuged at 9000 rad/min for 6 min. the product was dissolved in 4 mL cyclohexane, 8 mL ethanol was added and centrifuged at 9000 rad/min for 6 min. Repeat the previous step with 4 mL ethanol and 4 ml methanol instead of 8 mL ethanol. The resulting sample was dissolved in 5 mL cyclohexane sealed and stored in a glass vial at 4 ℃.

Shell precursor solution was prepared as the preparation method of core layer and cooled to room temperature. As-prepared nuclear solution was injected into precursor, NaOH and NH_4F mixed solution were added and incubated at 50 ℃ for 40 min. The sample was heated to 290 ℃ incubated for 2 h after the vacuum process. Original washing step was repeated to obtain the desired product. Dissolved in 5 mL of cyclohexane to be tested.

3.2.2 Characterization of the as-produced NCs

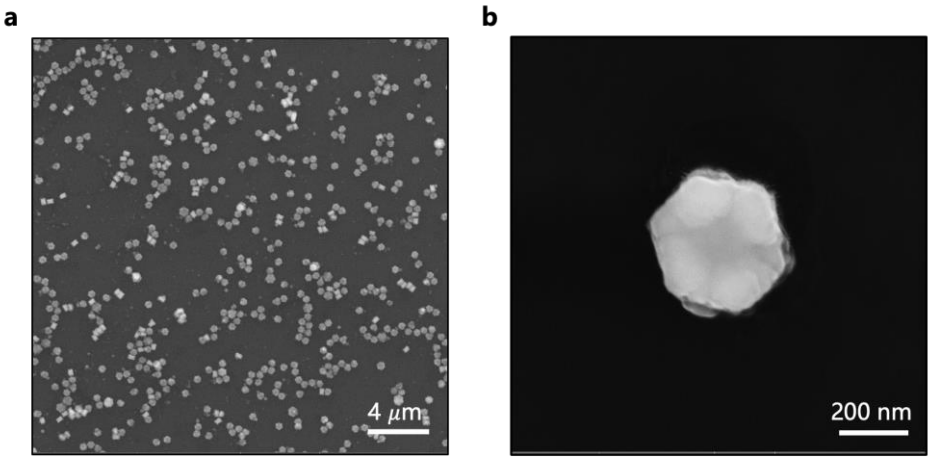

Supplementary Fig. S5 SEM images of the synthesised core-shell NCs

3.2.3 Energy-level diagram and the multistep upconverison process for a NC

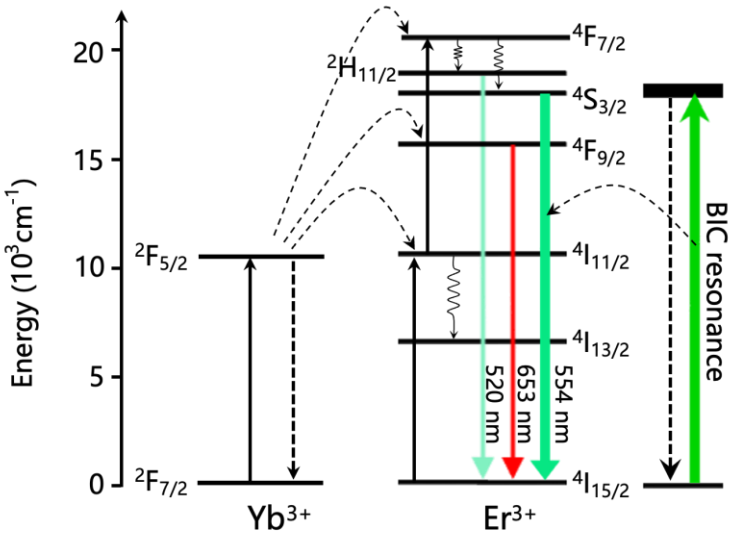

Supplementary Fig. S6. Energy level of Yb^{3+} and Er^{3+} ions relevant to the energy-transfer upconversion process.

The emission for luminescence up-conversion in Yb^{3+} and Er^{3+} co-doped $NaYF_4$ has been studied previously(*3–5*). The major processes are shown in S6. Due to the large absorption cross-section of Yb^{3+} and its higher doping concentration, most of the incident light is absorbed by Yb^{3+}, exciting it from the $^2F_{7/2}$ to $^2F_{5/2}$ state. Through an energy transfer process, the Yb^{3+} ion excites a nearby Er^{3+} ion into the $^4I_{11/2}$ state. Before returning to the ground state, another energy transfer occurs, which excites the Er^{3+} ion to the $^4F_{7/2}$ level. Then, a non-radiative transition to the $^2H_{11/2}$ and $^4S_{3/2}$ states, the ions return to the ground state $^4I_{15/2}$, emitting green luminescence. The multi-BIC resonance supported by the TPC exhibits spectral overlap with the $^4S_{3/2}$ excited state emission of Er^{3+}-doped upconversion nanoparticles. A fraction of Er^{3+} ions in the $^4S_{3/2}$ state would decay non-radiatively into the slightly lower $^4F_{9/2}$ level, followed by a transition back to the ground state, where red luminescence originates.

3.3 Deposition of single-NCs in topological plasmonic cavities

A 5 μL suspension of 400 nm NCs (5 mg/mL) was spin-coated onto the topological plasmonic cavity at a target speed of 4000 rpm. The spin-coating duration was 60 *s*, with the rotation speed ramping up to 4000 rpm within the first 10 s. We successfully placed an NC at the centre of the gap surrounded by four topological lattices. The SEM image is shown in S7**S7**.

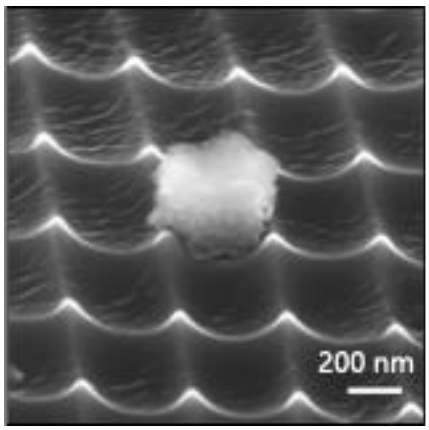

Supplementary Fig. S7 A cavity-emitter system formed by the coupling of a single-NC with a particle size of 400 nm and a topological plasmonic cavity.

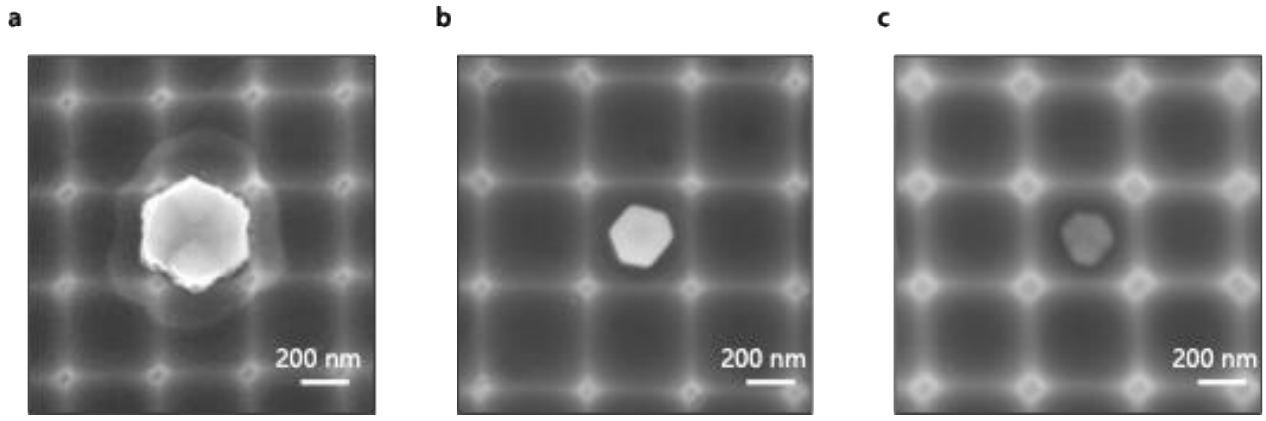

Supplementary Fig. S8 Using the same spin-coating protocol, single-NCs of different sizes were readily coupled into the topological plasmonic cavity: **a,** 400 nm NC. **b,** 300 nm NC (5 mg/mL) at 4000 rpm, and **c,** 200 nm NC (3 mg/mL) at 4000 rpm.

4. Experimental setup

4.1 Common optical path for angle-resolved resonance scattering and photoluminescence

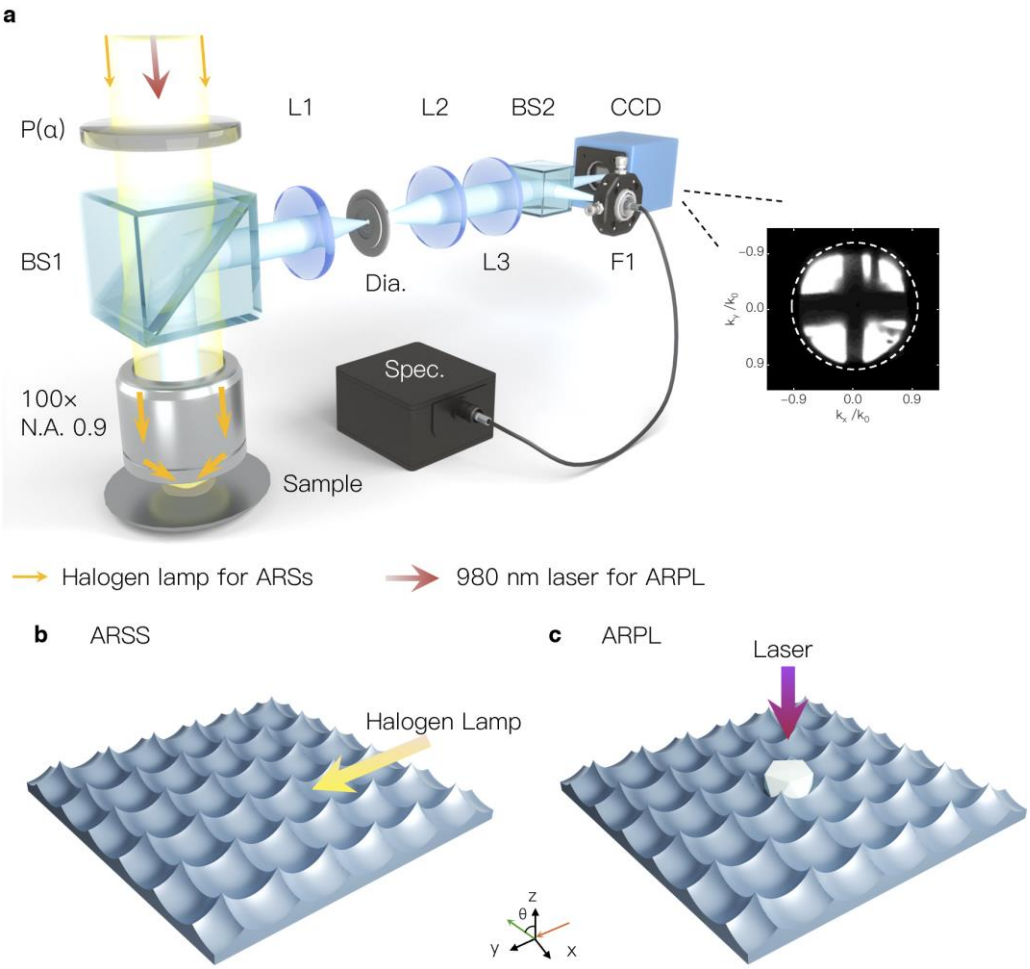

Supplementary Fig. S9. Detailed optical setup for angle-resolved scattering spectroscopy and photoluminescence spectroscopy measurements.

ARSS and ARPL were both based on a FBP imaging device. For ARSS measurements, the sample was excited using a halogen lamp as the incident light source. A rotatable adjustable mount with a linear polarizer was used to adjust the direction of polarization of the incident light along the *y*-direction before it entered the beam-splitting prism. A dark field module (model) was used to project the incident light field onto a 100× Olympus objective that was corrected for high numerical aperture (NA = 0.9) and infinite conjugate and incident at a large angle to the sample surface. The diffracted light from the sample was collected by the same objective lens and directed into a 4f optical system, comprising three lenses and a diaphragm. The incident light field uniformly illuminated the entire field of view under the 100× objective. To ensure the collected signals originated strictly from the structured area, an adjustable field diaphragm was strategically placed within the collection path. By precisely

controlling the aperture size, the signal detection area was confined to a localized region of 8×8 lattice periods. This spatial filtering effectively eliminated background interference from the surrounding unpatterned substrate and ensured that the measured optical responses specifically reflected the properties of the designed topological nanocavity array.

Finally, the Fourier plane of the diffracted light was projected via beam splitter BS2 onto CCD (QImaging Retiga R1 from Cairn Research) and fiber spectrometer (Exemplar®Plus, BTC655N). We used fiber with a core diameter of 100 μm (model) to collect spectral signals displayed as spots on the Fourier plane. The collection end of the fiber was fixed on a support rod connected to an electric displacement platform, enabling point-by-point scanning with a 0.1 mm step using an externally-drive system to achieve dispersion imaging of the sample in momentum space. This configuration effectively eliminated scattered light interference from other positions around the sample, ensuring precise and focused light collection to produce sharp resonance peaks. Converting L3 into a lens with a focal length twice that of L3 allows for fast switching between momentum space and real space imaging. The ARPL measurements were performed with the same optical setup, using a 980 nm laser to vertically excite a single NC. After the PL signal of the sample is passed through an 800 nm short pass filter (placed in front of the L1), the Fourier image and the ARPL spectrum of the signal are imaged simultaneously using an FBP device.

4.2 Micro-area measurement of upconversion lifetime for single-NCs

The time-resolved confocal microscope (MicroTime 200, PicoQuant) was used to capture the fluorescence lifetime of individual upconversion nanocrystals (UCNCs). A picosecond pulsed diode laser (LDH-D-C-980, PicoQuant) with a wavelength of 980 nm was used as an excitation source and controlled via a programmable laser driver (PDL 828 “Sepia II”, PicoQuant). The excitation radiation was transferred into an oil-immersion objective lens (100×, NA = 1.4, Olympus) via a dichroic mirror and concentrated onto the sample mounted in a high-precision piezoelectric scan stage. The upconversion luminescence (UCL) emitted from the sample was collected by the same objective and passed through a band-pass filter (center wavelength: 582 nm, Full Width at half maximum:75 nm) to effectively remove the residual excitation light. The filtered signal was then focused onto a confocal

pinhole to ensure spatial resolution and directed to a Single Photon Avalanche Photodiode (SPAD, PMA Hybrid, PicoQuant). The detected photon events were time-tagged and analyzed by a time-correlated single-photon counting (TCSPC) module (HydraHarp 400, PicoQuant), enabling high-resolution fluorescence lifetime measurements. The MicroTime 200 system was operated under SymPho Time 64 software, which provides lifetime fitting and photon correlation analysis. This configuration allows for spatially resolved lifetime imaging and spectral characterization of individual nanocrystals, enabling a detailed analysis of their local photophysical properties under up-conversion excitation.

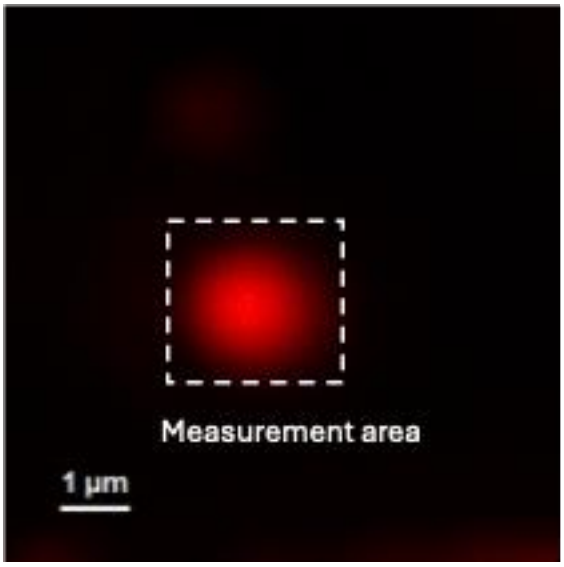

Supplementary Fig. S10. Confocal image of bright emission from a single-NC filled in a TPC under 0.2 MW power excitation at 976 nm.

5. TPC high-Q multi-BIC mode emission cone overlaps with upconversion emission cone on single-NC in cavity

As shown in the schematic diagram in S9b, the TPC is excited by a halogen lamp at a large incident angle using a 100× dark-field objective lens (numerical aperture NA = 0.9). The TPC's momentum-space emission image is captured by an infinite-corrected 4*f* optical system equipped with a 532 nm bandpass filter. The momentum space equal-frequency contours are shown in S11a. The Fourier transform of the back-focus plane image reveals a horizontal slice of the high-Q multimode BIC mode emission cone at the 532 nm emission wavelength. Four mode arcs are observed,

corresponding to the wave vectors of the square lattice, with their intersection points marking the M point of the topological plasmonic lattice.

Using the optical setup shown in S9a,c, single-NC in the TPC was pumped with 980 nm incident light. The coupled polariton emission cone was captured on the Fourier back focal plane image. The emission cone has similar momentum space distribution characteristics to the multimode BIC emission cone of the TPC.

ARRS and scattering analysis provide direct experimental evidence for the existence of multi-BIC states within the TPC. As shown in Fig. 3c, the TPC supports distinct high-Q singularities where radiative leakage is suppressed, identified at the Γ point and at off-axis symmetry-protected positions near 30°. The divergence of the Q factor at these specific momentum-space coordinates signifies the formation of a multi-BIC framework, where the coupling between different resonance modes leads to the complete suppression of the radiation channel.

This is further verified by the angle-resolved scattering spectrum at a fixed angle of 30° (S12). The measured spectral profile exhibits a pronounced resonant dip (blue arrow), serving as a definitive signature of destructive interference between two coupled resonance modes. This spectral feature confirms the formation of a FW-BIC at this non-Γ position. The observation of both symmetry-protected BICs and off-axis FW-BICs experimentally validates the presence of the multi-BIC distribution, providing the high-Q environment necessary for advanced light-matter interaction.

The directionality is determined by the cooperative modulation of multi- BICs. As shown in S12, q-BIC and FW-BIC act as radiative singularities at the Γ point and off-Γ point, respectively, with vanishing attenuation rates, where emission is forbidden. Therefore, upconversion radiation is reconfigured and directed to low-Q radiative regions surrounding these singularities. This mechanism confines the emission branches within specific angular windows, leading to the sharp momentum space features observed in the experiment (S13).

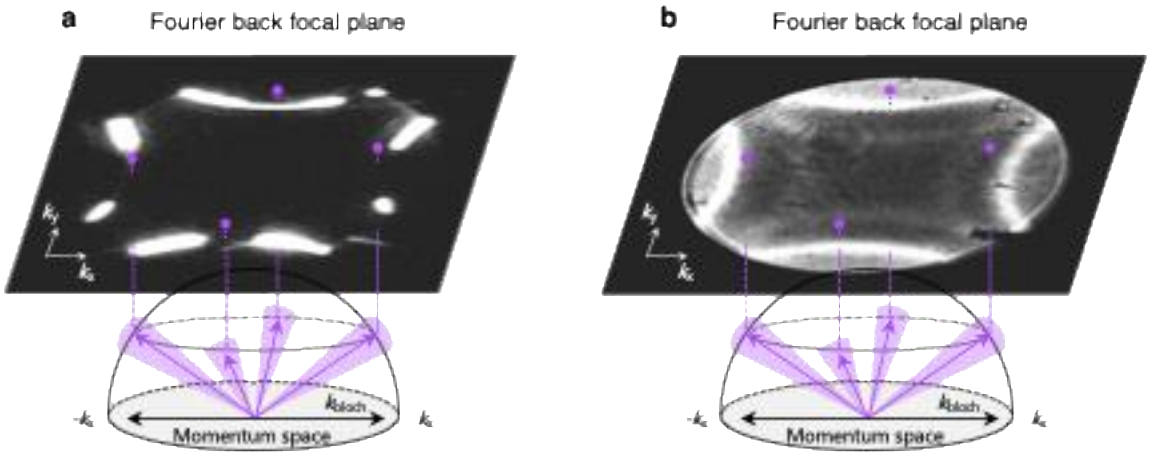

Supplementary Fig. S11. a, FBP image of the TPC under large-angle dark-field illumination (NA = 0.9) excited by a halogen lamp. The momentum space emission signal filtered at 532 nm shows a high-Q multimode BIC radiation pattern. The four crescent-shaped arcs correspond to the diffraction Bloch modes of the square lattice, with their intersection points marking the M point in momentum space. **b,** FBP image of a single-NC coupled to the TPC under 980 nm excitation. The observed emission cone exhibits a similar feature distribution to the intrinsic multimode BIC profile of the TPC, indicating overlap between the NC and the underlying multi-BIC modes.

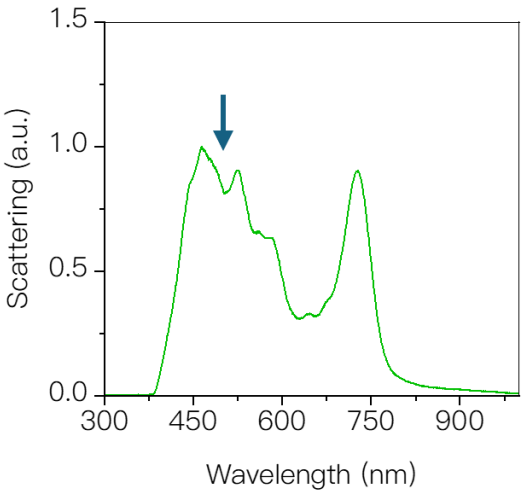

Supplementary Fig. S12 Spectra of off-Γ FW BICs. Representative raw scattering spectrum extracted at θ = 30° from the TPC lattice. The characteristic dip indicated by the blue arrow results from destructive interference (strong coupling) between two resonance modes, confirming the formation of an off-Γ FW-BIC at this coordinate. This non-radiative topological "anchor" suppresses leakage at the designated angle, thereby precisely directing the PL emission into the predicted directional channels.

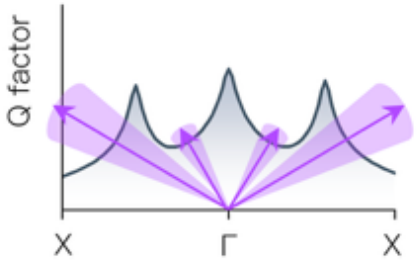

Supplementary Fig. S13. Schematic of multi-BIC directional control.

6. Extraction of the Purcell factor of single-NCs with different particle sizes from the change in upconversion lifetime

6.1 PL spectra of different NC sizes

To achieve efficient light-matter interaction, the TPC nanocavity is engineered to satisfy both spectral and spatial matching with the upconversion nanocrystals (UCNPs). Since the emission peaks of Er^{3+}/Yb^{3+} co-doped UCNPs are intrinsically fixed at 550 nm and 650 nm regardless of particle diameter (S14), the nanocavity is designed with a quasi-BIC resonance tuned to these wavelengths, providing a universal enhancement platform for all tested emitter sizes.

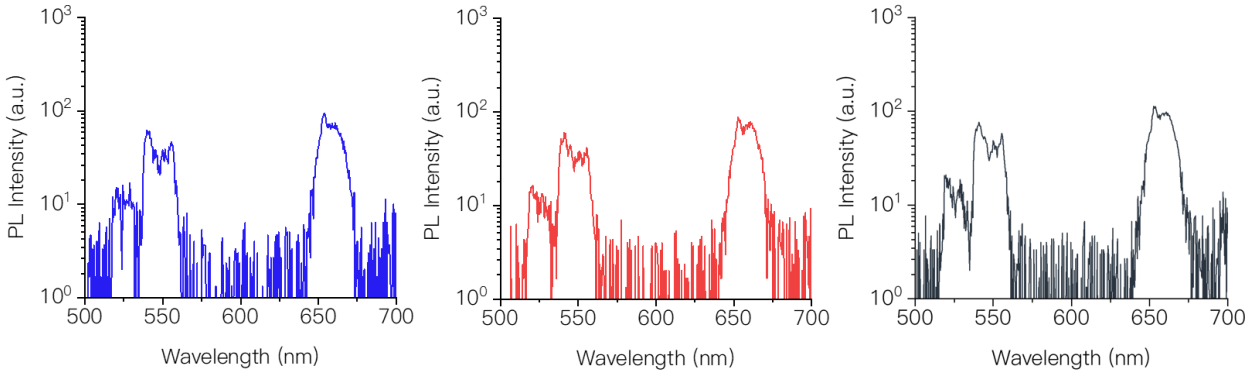

Supplementary Figure S14. Spectral consistency of UCNPs with different diameters.

The study of varying diameters (200–400 nm) highlights a trade-off between surface quenching and spatial occupancy. While smaller NCs suffer from severe non-radiative quenching due to high surface-to-volume ratios, the 400 nm NCs maintain a substantial "protected" active core. Furthermore, as NCs statistically settle on the cavity floor rather than the tips (Fig. 4b), the BIC mode's distributed field enhancement across the base ensures an optimized spatial match. This balances a large active

luminescent volume with the topological mode, maximizing the volume-integrated emission.

6.2 PL Extract Purcell factor from lifetime

The UCL dynamics in sensitizer-activator co-doped NCs under weak excitation are governed by the following rate equations:

$$\frac{d}{dt}n_{S_1} = \varphi_0 n_{S_0} - \Gamma_r^S n_{S_1} - (\omega_0 n_{A_0} + \omega_1 n_{A_0}) n_{S_1} \tag{S1}$$

$$\frac{d}{dt}n_{A_1} = \omega_0 n_{S_1} n_{A_0} \square \omega_1 n_{S_1} n_{A_1} \square n_{A_1}/\tau_1^A \tag{S2}$$

$$\frac{d}{dt}n_{A_2} = \omega_1 n_{S_1} n_{A_1} - (\Gamma_r^A + \Gamma_{nr}^A) n_{A_2} \tag{S3}$$

where n_{S_i} (in m^{-3}) and n_{A_i} (in m^{-3}) denote population densities of sensitizer (e.g., Yb^{3+}) and activator (e.g., Er^{3+}) energy states $\varphi_0 = \sigma_S \rho/h\nu$ is the sensitizer absorption rate (σ_S:absorption cross-section, ρ: excitation power density) Γ_r^S, Γ_r^A are radiative decay rates, Γ_{nr}^A is the nonradiative decay rate ω_0, ω_1 represent Yb→Er energy transfer coefficients

The UCL decay is bottlenecked by the Yb^{3+} energy level $^2F_{5/2}$ state relaxation:

$$\tau_0^{Yb} = (\Gamma_r^{Yb} + w_0 n_A)^{-1} \tag{S4}$$

The down-conversion luminescence (DCL) lifetime reflects the activator's metastable state decay:

$$\tau_0^A = (\Gamma_r^A + \Gamma_{nr}^A)^{-1} \tag{S5}$$

When coupled with a nanocavity, τ_0^{Yb} and τ_0^{Er} will be shortened by the nanocavity to be

$$\tau_{cav}^{Yb} = (F_P^{980}\Gamma_r^{Yb} + w_0 n_A)^{-1} \tag{S6}$$

$$\tau_{cav}^{Er} = (F_P^{\lambda_{em}}\Gamma_r^{Er} + \Gamma_{nr}^{Er})^{-1} \tag{S7}$$

The decay dynamics of UCL are primarily governed by the Yb^{3+} sensitizer lifetime. That is, the measured UCL lifetimes approximate the Yb^{3+} decay time:

$$\tau_0^U \approx \tau_0^{\mathrm{Yb}}, \quad \tau_{\mathrm{cav}}^U \approx \tau_{\mathrm{cav}}^{\mathrm{Yb}} \tag{S8}$$

The UCNP coupled with the topological nanocavity exhibits simultaneously shortened decay

times and significantly enhanced luminescence. As the observed emission is a collective summation of discrete Er^{3+} ions within the 400 nm nanocrystal, ions near the nanocone surfaces experience much stronger Purcell enhancement and accelerated radiative rates compared to those in the core. Consequently, the transient kinetics follow a two exponential decay model:

$$I(t) = Aexp\left(-\frac{t}{\tau_{cav}}\right) + Bexp\left(-\frac{t}{\tau_{cav'}}\right) \tag{S9}$$

where *I(t)* is the luminous intensity, *t* is the attenuation time, A and B are the two amplitudes obtained by double exponential fitting, corresponding to the fast and slow decay components respectively. τ_{cav} and $\tau_{cav'}$ are fast and slow time constants respectively (S15)

according to Eq. (S8), we can express F_P^{980} with τ_{cav}^{U} as

$$F_{\mathrm{P}}{}^{980} = [(\tau_{\mathrm{cav}}{}^{\mathrm{U}})^{-1} - w_0 n_{\mathrm{Er}}]/\Gamma_{\mathrm{r}}^{\mathrm{Yb}}, \tag{S10}$$

Noting that $W_0 n_{\mathrm{Er}}$ is extracted from the measured τ_0^U via $w_0 n_{\mathrm{Er}} = \left(\tau_0{}^{\mathrm{U}}\right)^{-1} - \Gamma_{\mathrm{r}}^{\mathrm{Yb}}$, we may also express F_P^{980} as

$$F_{\mathrm{P}}{}^{980} = \left[(\tau_{\mathrm{cav}}{}^{\mathrm{U}})^{-1} - \left(\tau_0{}^{\mathrm{U}}\right)^{-1}\right]/\Gamma_{\mathrm{r}}^{\mathrm{Yb}} + 1. \tag{S11}$$

Therefore, we can extract F_P^{980} from the measured UCL lifetime change, with the related parameters summarized in Table S1.

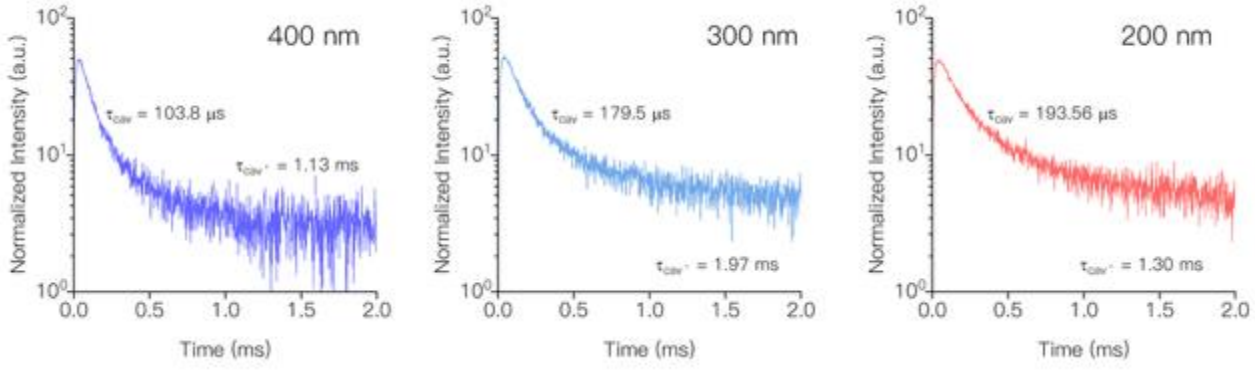

Supplementary Fig. S15. Luminescence decay time of different particle size UC coupled with TPC

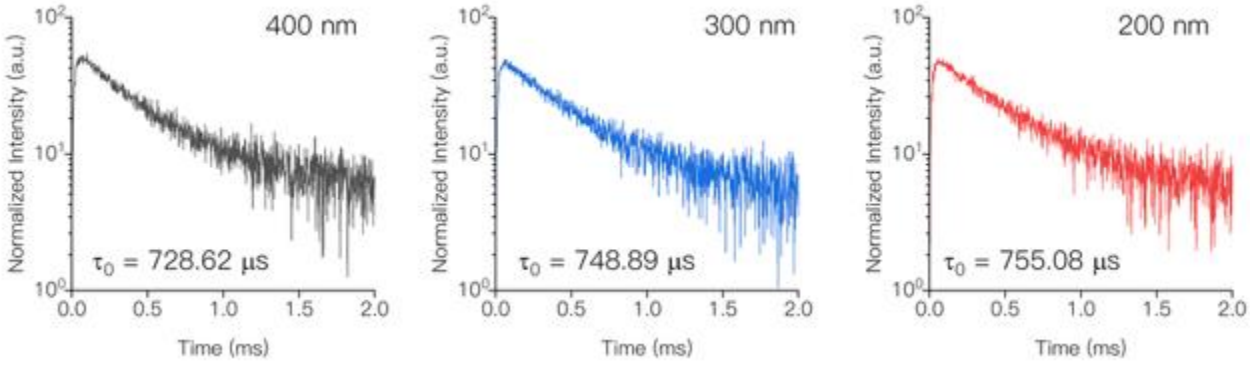

Supplementary Figure S16. Size-dependent PL decay dynamics of UCNPs on a reference flat substrate.

NC Size (nm)	$\tau_{cav}{}^{U}$ (μs)	$\tau_0{}^{U}$ (μs)	Γ_r^{Yb} (s^{-1})
200	193.56	756.08	476.2
300	179.51	748.89	476.2
400	103.82	728.62	476.2

Supplementary Table S1. Summary of key physical parameters for extracting the effective Purcell factor.

7. Topological properties of plasmonic lattice band

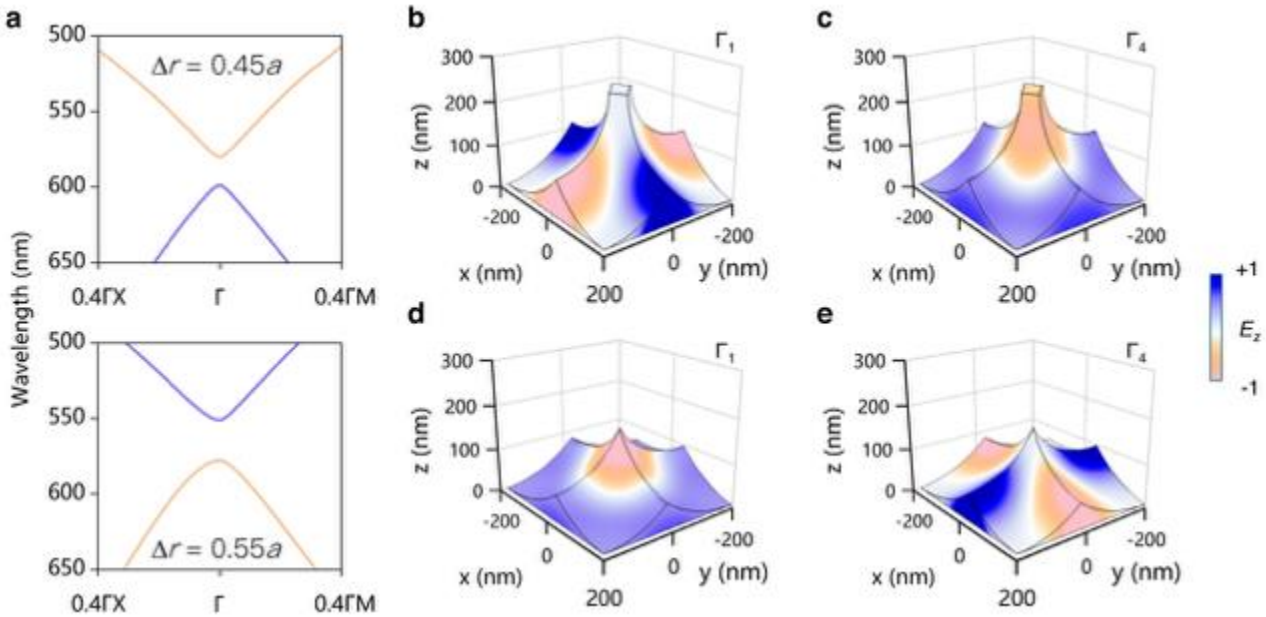

Supplementary Fig. S17. Zak phase transition and modal inversion in plasmonic lattices. a, Calculated 2D Zak phases of the lower and upper bands in the uncompressed (top) and compressed (bottom) plasmonic lattices. **b,c,** E_z field distributions at the Γ point in the uncompressed lattice show a quadrupole mode (Γ_1) in the lower band and a monopole mode (Γ_4) in the upper band. **d,e,** Corresponding modal profiles in the compressed lattice exhibit inversion of these modes, confirming the topological phase transition.

We briefly discuss the band topology properties of plasmonic lattices after introducing sigma symmetry breaking. Considering the evolution of the unit cell from uncompressed ($\Delta r < 0.5a$) to compressed ($\Delta r > 0.5a$) as shown in Figure 1c of the main text, we observe that the accidental intersection points in the band structure undergo a process of closing and reopening (Figs. 2b,c), which is similar to the topological engineering of band structures in one-dimensional dielectric photonic crystals. To reveal the topological properties of the plasmonic lattice's energy bands, we theoretically investigated topological band inversion in the system. By gradually varying the lattice compression factor Δr, we observed topological band inversion, corresponding to a geometric phase shift in the mixed energy bands (S17**S17**). This topological phase transition induced by $\boldsymbol{\sigma_h}$ symmetry breaking can be characterized by the two-dimensional Zak phase, defined as follows:

$$\theta_\alpha = 2\pi \mathbf{P}_\alpha = \frac{1}{2\pi} \int_{\mathrm{FBZ}} \mathrm{Tr}\left[A_\alpha(\mathbf{k})\right] \mathbf{dk}, \quad \alpha = x, y, \tag{S12}$$

where $\mathbf{P} = [Px, Py]$ indicates the 2D polarization of the lattice, $A_a(\mathbf{k}) = i \langle \psi_{n,k} | \partial_{k_a} | \psi_{n,k} \rangle$ is the Berry connection, and $|\psi_k\rangle$ denotes the Bloch eigenfunction on the *n*th band with wave vector *k*. We chose the Γ point of the plasmonic lattice as the inversion center to calculate the two-dimensional Zak phases, as shown in S17a. In the uncompressed lattice (top panel), the lower and upper bands are characterized by Zak phases of (π, π) and (0, 0), respectively. Upon compression (bottom panel), a clear topological transition is observed: the Zak phases of the lower and upper bands switch to (0, 0) and (π, π), respectively, confirming a band inversion. The topologically nontrivial bands are highlighted by purple lines (S17a). At the critical state (Fig. 2b in the main text), the bandgap closes and the Zak phase becomes ill-defined, consistent with a topological phase transition. This transition is further corroborated by the observed modal inversion. As shown in Figs. S16b and S16c, the 3D electric field distributions (E_z) at the Γ point in the uncompressed lattice reveal a quadrupolar mode in the lower

band (Γ_1) and a monopolar mode in the upper band (Γ_4). In contrast, the compressed lattice exhibits an inversion of these modal profiles (Figs. S16d and S16e), further confirming the band inversion.

Notably, the q-BIC mode in the undeformed/uncompressed lattice consistently appears in the band hosting the quadrupolar mode (S18). The observed band inversion indicates that the in-plane Bloch wave of the plasmonic lattice accumulates an additional geometric phase as the system parameters are tuned continuously. This behavior arises from strong coupling between the Bloch wave and LSPR, giving rise to plasmonic lattice resonances.

8. Dispersive characteristics of uncompressed cavity

Here we supplement the undeformed cavity's dispersion characteristics not given in the main text, where S18a shows the 3D photonic band structure of the undeformed cavity, and S18b and c are ARSS and ARRS, respectively. respectively.

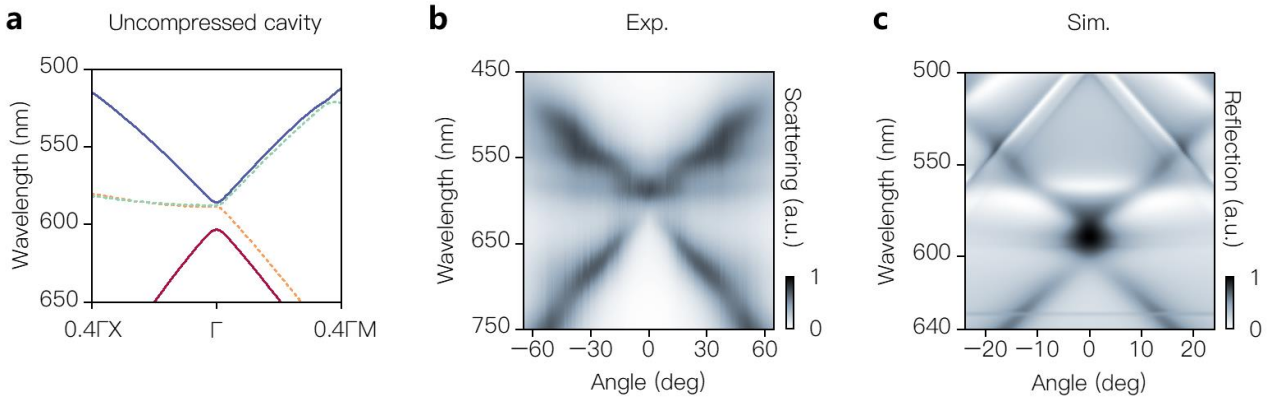

Supplementary Fig. S18. Photonic band structure (a), ARSS (b) and ARRS (c) of an uncompressed lattice ($\Delta r = 0.45a$)

9. Comparative Analysis of Mode Robustness and Stability

To evaluate the functional superiority of the topological plasmonic cavity (TPC), we performed comparative simulations between a topologically trivial, uncompressed supercell and the TPC under emitter-induced perturbations. As illustrated in Figures S18a and S18b, while the trivial supercell at BIC resonance initially exhibits a well-defined quadrupole mode, the introduction of a single NC significantly disturbs and fragments the E_z field profile. This susceptibility to local dielectric

perturbations is a direct consequence of the trivial lattice's inability to maintain resonance integrity under spatial constraints.

In stark contrast, the TPC demonstrates remarkable immunity to such impurities. As shown in Figures S18c and S18d, the E_z field distribution of the TPC supercell remains nearly identical before and after the coupling of a single NC. This preservation of the localized field characteristics and mode symmetry, even in the presence of an emitter-induced perturbation, highlights the inherent topological robustness of the TPC. This decisive functional edge confirms that the TPC provides a more stable and efficient framework for light-matter interaction compared to conventional, non-topological plasmonic designs, ensuring that the cavity resonance remains robust against scattering and local dielectric changes.

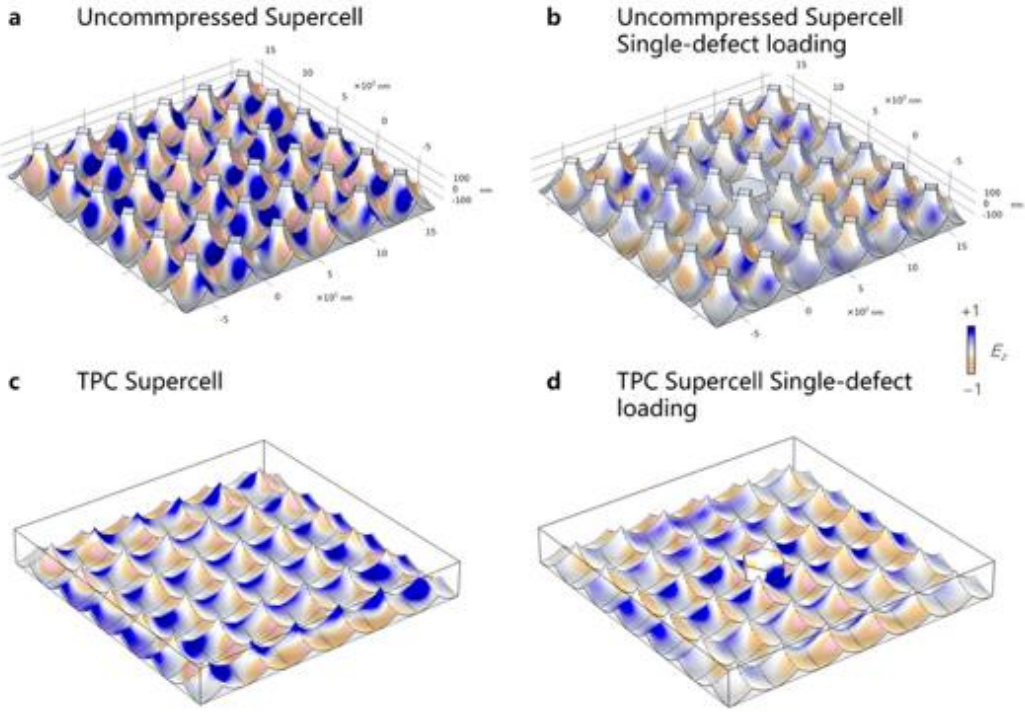

Supplementary Fig. S19. **Mode stability comparison between trivial and topological lattices.** (a-b) E_z field distribution of a trivial uncompressed supercell (a) without and (b) with a single NC, showing a fragmented and unstable mode profile. (c-d) E_z field distribution of the TPC supercell (c) without and (d) with a single NC, demonstrating topological robustness and immunity to emitter-induced perturbations.

10. Single-NC upconversion far-field radiation direction comparison inside and outside the TPC

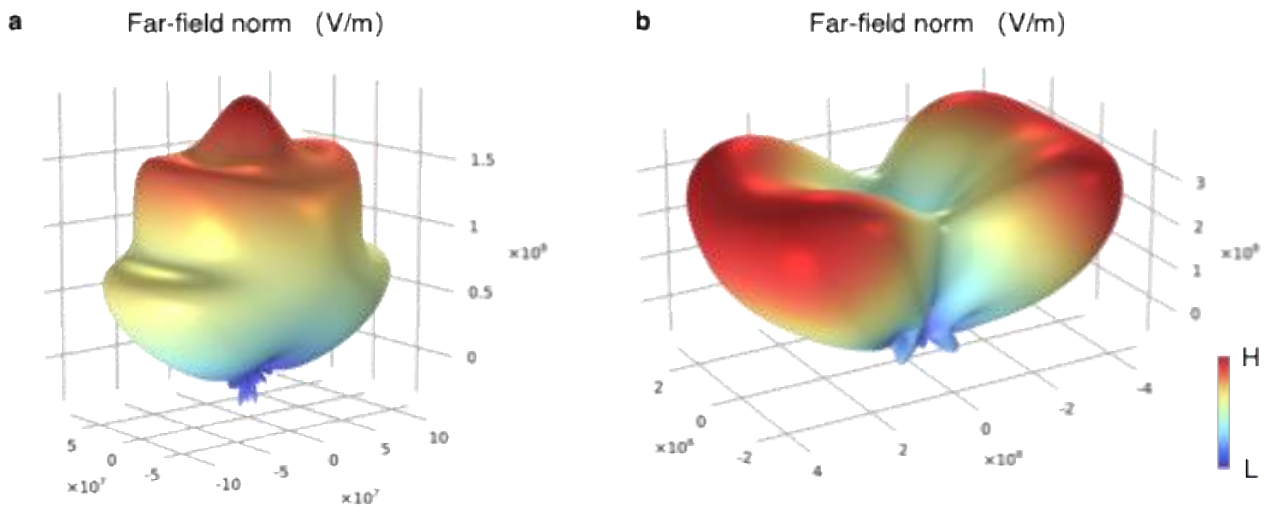

Supplementary Fig. S20. Comparison of far-field radiation patterns for single-NC upconversion emission simulated in COMSOL. A dipole source oriented along the *x*-axis was used to model the emission from a single-NC **a,** Radiation pattern of the NC placed directly on a flat aluminum film, representing the uncoupled case. The emission is broadly distributed in multiple directions with no clear confinement, indicating inefficient free-space coupling. **b,** Radiation pattern of the same NC embedded within a topological plasmonic cavity (TPC). A highly directional emission profile is observed, concentrated into lobes orthogonal to the dipole orientation, consistent with coupling to finite Q multi-BIC modes supported by the TPC. The color scale represents the normalized electric field strength in the far field (*V/m)*, with H and L denoting high and low intensity, respectively.

To compare the enhancement strength, the photoluminescence intensity was integrated along the X–Γ–X trajectory in momentum space, as illustrated in Fig. S21a. This integration path intersects the four radiation hotspots associated with the TPC emission cone. For NC coupled to the TPC cavity, the emission is preferentially concentrated within these directional channels, whereas the emission from NCs on a flat Al substrate is distributed over momentum space without preferred directions. As shown in Fig. S21b, despite sampling only a narrow trajectory in momentum space, the cavity-coupled NC exhibits more than a twofold enhancement of the 550 nm emission compared with the reference NC

on the flat substrate. This result further confirms the efficient redistribution and enhancement of spontaneous emission enabled by the q-BIC cavity.

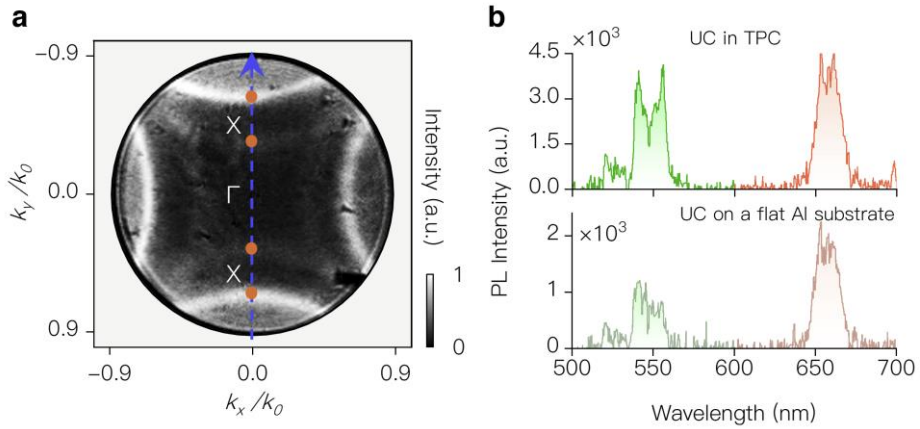

Supplementary Fig. S21. (a) Momentum-space image showing the X–Γ–X trajectory (blue dashed line) used for angle integration. The integration path passes through the four radiation hotspots associated with the TPC emission cone. (b) Angle-integrated ARPL spectra extracted along the X–Γ–X trajectory for a nanocrystal inside the TPC cavity (top) and a reference nanocrystal on a flat Al substrate (bottom).

11. Emission Characteristics of a Single UCNP on a Flat Aluminum Film

To establish a baseline for evaluating the beam-shaping performance of the topological plasmonic cavity, we first characterized the emission properties of an isolated upconversion nanoparticle (UCNP) in the absence of any photonic lattice. A single UCNP (approximately 400 nm in diameter) was dispersed on a flat, unpatterned aluminum film. S22a shows the Fourier-plane (momentum-space) image of the upconversion luminescence (UCL) under continuous-wave excitation at 980 nm. The emission displays a nearly isotropic distribution, indicating that without the topological cavity, the emitted light lacks any spatial confinement or directional preference.

The corresponding ARPL spectrum along the high-symmetry direction (X–Γ–X) is presented in S22b. Three characteristic emission peaks of Er^{3+} ions are clearly identified at 525 nm ($^4F_{7/2}\rightarrow{}^4I_{15/2}$), 550 nm ($^4S_{3/2}\rightarrow{}^4I_{15/2}$), and 650 nm ($^4F_{9/2}\rightarrow{}^4I_{15/2}$). These emissions are distributed across a broad angular range from –60° to +60°, with the maximum intensity observed around ±25°. This angular profile is consistent with electric dipole-type radiation on a metallic surface and confirms the presence of only low -Q emission channels in the absence of the topological BIC mode.

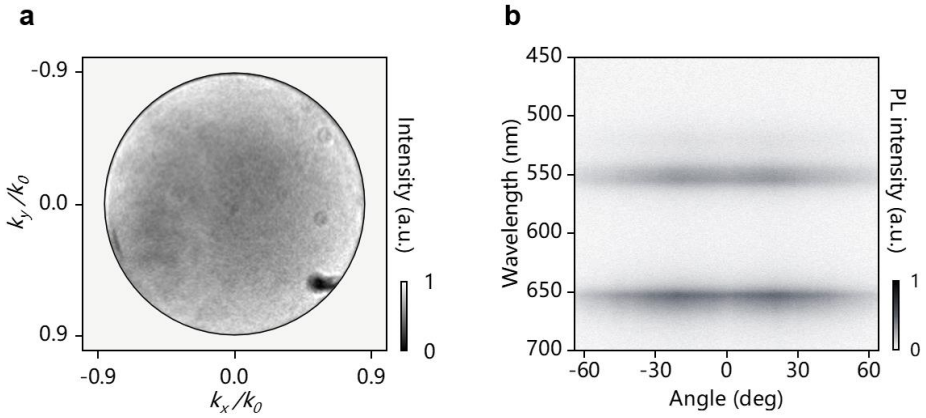

Supplementary Fig. S22. a, Fourier-plane image of the upconversion luminescence (UCL) from a single 400 *nm* upconversion NC placed on a flat aluminum film. The isotropic angular distribution confirms the absence of photonic confinement or directional coupling. **b**, Angle-resolved PL spectrum of the same NC along the high-symmetry X–Γ–X direction, showing three emission peaks (525 *nm*, 550 *nm*, 650 *nm*) attributed to Er^{3+} transitions. Emission extends broadly (±60°), consistent with dipolar radiation in free space.

12. Experimental Decoupling of BIC and LSPR Contributions

To quantitatively distinguish the individual contributions of the topological BIC and the LSPR to the overall upconversion enhancement, we performed control experiments using disordered nanocone arrays. The core design of our lattice architecture relies on breaking out-of-plane symmetry to induce a dual-enhancement mechanism, where the q-BIC mode (characterized by a high, finite-Q factor) and the high-LDOS nanocone plasmonic modes are spectrally and spatially aligned.

While these two phenomena are synergetically intertwined in the perfectly periodic TPC, their contributions can be isolated by disrupting the lattice periodicity. We fabricated a series of nanocone arrays with increasing degrees of spatial disorder (Figs. S22a–c), which eliminates the collective BIC mechanism while preserving the individual nanocone geometry and its associated LSPR effects.

As shown in the PL spectra (Fig S22d), the baseline enhancement provided solely by the localized hotspots of the disordered nanocones is approximately 23-fold compared to a flat substrate. In contrast, statistical measurements reveal that the perfectly periodic TPC platform achieves an average enhancement of 120-fold, reaching a peak of 147-fold. This comparison reveals that while the localized plasmonic fields provide a substantial foundation for light-matter interaction, the primary driver for

the unprecedented brightness is the synergistic dual-mode coupling. Specifically, the high-Q BIC mode further amplifies the localized fields of the nanocones, contributing an additional average enhancement of ~5.2-fold (and up to ~6.4-fold) beyond the LSPR limit. This experimental evidence confirms that the seamless overlap of topological and plasmonic modes is the cornerstone of our strategy for boosting single-nanoparticle upconversion.

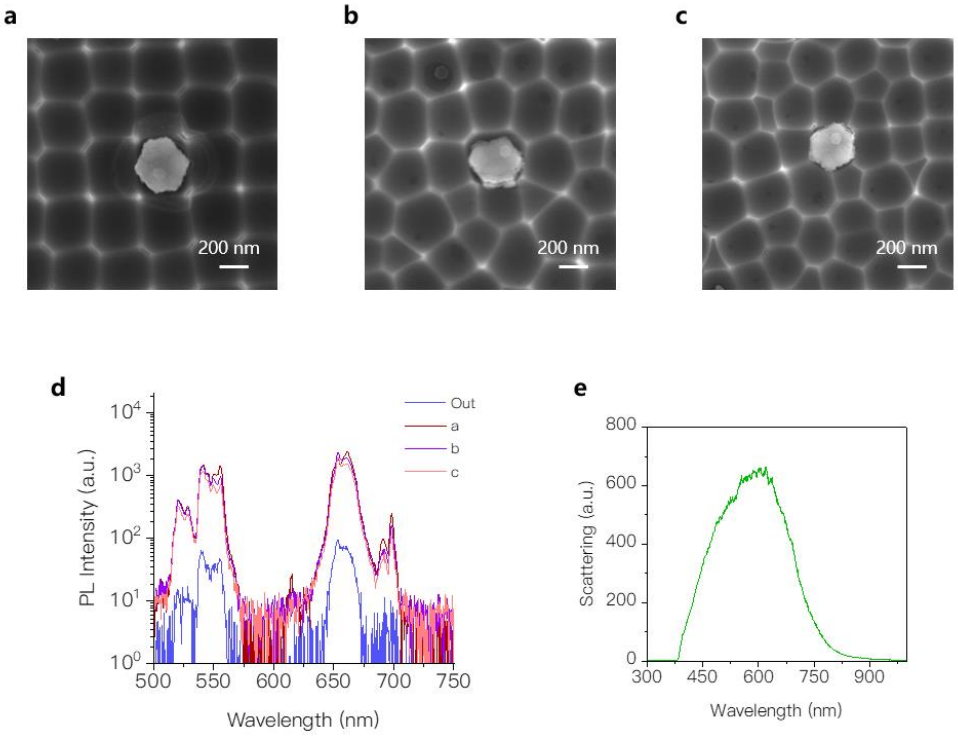

Supplementary Fig. S23. Decoupling of LSPR and topological BIC enhancement mechanisms. (a–c) SEM images of the fabricated nanocone arrays with increasing degrees of spatial disorder, where the lattice periodicity is systematically disrupted while maintaining identical individual nanocone geometry. (d) Representative PL spectra of a single 400 nm UCNP coupled to a flat substrate (reference), a disordered nanocone array (23-fold LSPR-only enhancement), calculated values from the peak contrast at 555 nm. (e) The scattering spectrum without BIC in the disordered lattice shows LSPR characteristics.

13. Experimental Comparison Between Mode-Coupled and Non-Coupled PL Components

To directly evaluate the efficacy of the TPC, we performed an internal comparison between the mode-coupled (directional) and non-coupled (vertical) PL components within the same measurement.

As illustrated in S33, the PL signal at the Γ point is extremely weak, representing the near-complete suppression of vertical radiative leakage due to the symmetry-protected BIC.

In stark contrast, the emission is overwhelmingly concentrated within the engineered off-axis topological channels. This high directional contrast ratio demonstrates that the TPC effectively funnels the upconversion light away from the vertical axis and into the high-Q directional branches. This comprehensive comparison provides definitive experimental evidence that the observed PL enhancement and directionality are not generic features, but are strictly governed by the radiative boundaries defined by the multi-BIC framework.

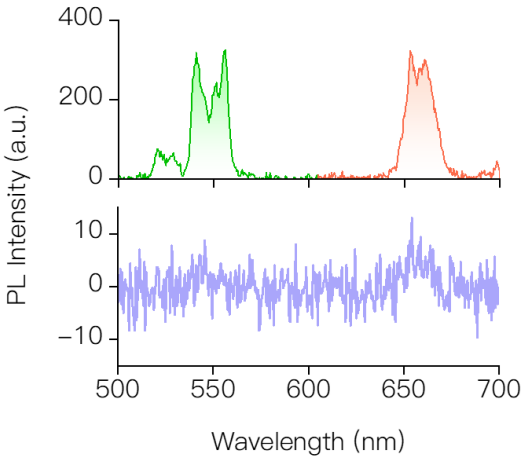

Supplementary Fig. S24. PL spectra comparison between coupled and non-coupled modes. (Top) Real-space PL spectrum extracted from the mode-coupled directional branch (off-axis), showing intense emission within the engineered topological channels. (Bottom) PL spectrum measured from the non-coupled component (vertical emission at the Γ point), exhibiting an extremely weak signal due to BIC-induced radiative suppression.

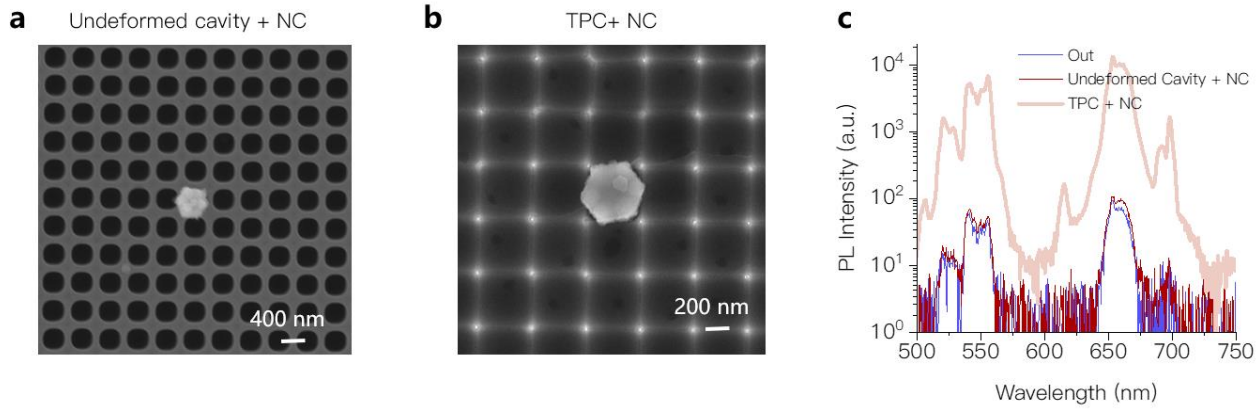

Supplementary Fig. S25. PL enhancement comparison between the undeformed cavity and TPC for a single NC

Reference

1. J. Zheng, Z. Yang, Y. Guo, Y. Fang, A Detailed Investigation in the Enhancement Factor of Surface-Enhanced Raman Scattering in Simulation. *Plasmonics* **16**, 2207–2214 (2021).

2. F. Lv, J. La, S. He, Y. Liu, Y. Huang, Y. Wang, W. Wang, Off-Angle Amplified Spontaneous Emission of Upconversion Nanoparticles by Propagating Lattice Plasmons. *ACS Appl. Mater. Interfaces* **14**, 54304–54312 (2022).

3. Y. Yang, Y. Cong, X. Lin, B. Cao, D. Dong, K. Liu, Y. Xiao, J. Shang, Y. Bao, Y. Liu, G. Fang, Y. Wang, Y. Chen, J. Zhang, B. Dong, Dual LSPR of Au/W18O49 heterostructures for upconversion enhancement and application of molecular detection. *J. Mater. Chem. A* **8**, 4040–4048 (2020).

4. P. Zou, X. Hong, Y. Ding, Z. Zhang, X. Chu, T. Shaymurat, C. Shao, Y. Liu, Up-Conversion Luminescence of NaYF4:Yb3+/Er3+ Nanoparticles Embedded into PVP Nanotubes with Controllable Diameters. *J. Phys. Chem. C* **116**, 5787–5791 (2012).

5. M. T. Berry, P. S. May, Disputed Mechanism for NIR-to-Red Upconversion Luminescence in NaYF4:Yb3+,Er3+. *J. Phys. Chem. A* **119**, 9805–9811 (2015).